



HAL
open science

Resonant Triad Instability in Stratified Fluids

Sylvain Joubaud, James Munroe, Philippe Odier, Thierry Dauxois

► **To cite this version:**

Sylvain Joubaud, James Munroe, Philippe Odier, Thierry Dauxois. Resonant Triad Instability in Stratified Fluids. 2011. ensl-00616454v1

HAL Id: ensl-00616454

<https://ens-lyon.hal.science/ensl-00616454v1>

Preprint submitted on 22 Aug 2011 (v1), last revised 26 Apr 2012 (v2)

HAL is a multi-disciplinary open access archive for the deposit and dissemination of scientific research documents, whether they are published or not. The documents may come from teaching and research institutions in France or abroad, or from public or private research centers.

L'archive ouverte pluridisciplinaire **HAL**, est destinée au dépôt et à la diffusion de documents scientifiques de niveau recherche, publiés ou non, émanant des établissements d'enseignement et de recherche français ou étrangers, des laboratoires publics ou privés.

Resonant Triad Instability in Stratified Fluids

S. Joubaud¹, J. Munroe^{1,2}, P. Odier¹, T. Dauxois¹

¹*Laboratoire de Physique de l'École Normale Supérieure de Lyon,
CNRS & Université de Lyon, F-69364 Lyon, France,*

²*Department of Physics and Physical Oceanography,
Memorial University of Newfoundland, St. John's, NL A1B 3X7, Canada*

(Dated: July 26, 2011)

Internal gravity waves contribute to fluid mixing and energy transport, not only in oceans but also in the atmosphere and in astrophysical bodies. We provide here the first experimental measurement of the growth rate of a resonant triad instability (also called parametric subharmonic instability) transferring energy to smaller scales where it is dissipated. We make careful and quantitative comparisons with theoretical predictions for propagating vertical modes in laboratory experiments.

PACS numbers: 92.05.Bc, 47.35.Bb, 47.55.Hd, 47.20.-k

Internal gravity waves (IGW) result from the balance of inertia and buoyancy force in a density stratified fluid. Such waves have received a great deal of attention recently because of their relevance and ubiquity in different physical situations: they are believed to be of primary importance as they affect ocean mixing and energy transport [1]. Although internal waves do not play the dominant role in the evolution of weather and climate, their influence is non-negligible in the dynamics of the atmosphere [2]. IGW also exist in the solar radiative interior, generated at the interface between the convective and radiative regions, transporting angular momentum and are believed to produce observational signatures [3]. Moreover, the propensity of oceanic IGW to affect offshore oil and gas design, installation and operation is seriously being considered by oil companies [4].

From a fundamental point of view, these waves are also particularly intriguing. A striking consequence of stratification is an anisotropic dispersion relation relating the frequency to the direction of propagation of the wave and not to the wavelength. This property is also encountered for inertial waves (in presence of rotation) or plasma waves (in presence of a magnetic field). This has unexpected and interesting consequences in the propagation, reflection [5] or transmission properties of these waves [6].

Internal waves are known to be inherently unstable due to resonant triad instability [7], providing an efficient way to transfer energy from large to smaller scales, where it can be dissipated. This instability is often called parametric subharmonic instability since energy is transferred from a primary wave to two recipient waves at approximately half the frequency. Historically, a series of experiments were performed driving low-order standing modes with plungers on the sides of the container [8], with an oscillating paddle [9] or, more recently, relying on the parametric forcing of the tank [10]. For large amplitude forcing, some “irregularities” or “traumata” were observed, which led to mixing and overturning. Unfortunately no quantitative measurements were reported. We

report here on experiments performed with a wave generator that produces sinusoidal vertical waves propagating along a rectangular tank. We quantitatively measure the growth rate of the instability, a quantity of paramount importance to single out the major mechanism in dissipation processes, a recently highly debated issue [1, 11].

Theory.— Internal waves are characterized by the buoyancy frequency, $N = \sqrt{(-g/\rho_0)(d\rho/dz)}$, in which g is the acceleration of gravity, ρ_0 the characteristic fluid density and $(d\rho/dz)$ the density gradient in the vertical direction z . At large Prandtl number, the 2-D Boussinesq equations of motion can be written as

$$\frac{\partial^2 \nabla^2 \psi}{\partial t^2} + N^2 \frac{\partial^2 \psi}{\partial x^2} = \frac{\partial}{\partial t} J(\psi, \nabla^2 \psi) - \frac{g}{\rho_0} \frac{\partial}{\partial x} J(\rho', \psi) + \nu \nabla^4 \psi_t \quad (1)$$

where ρ' is the perturbation density field, ψ the stream function, J the Jacobian operator and ν the viscosity. Seeking wave solutions with wave number $\vec{k} = (k, m)$, Eq. (1) leads to the inviscid linear dispersion relation for frequency ω ,

$$\omega^2 = N^2 \frac{k^2}{k^2 + m^2}. \quad (2)$$

For small amplitudes, it can be assumed that that several waves could concurrently exist simply as a linear superposition. However, in the case of a resonant triad interaction, where three waves satisfy the spatial resonance condition

$$\vec{k}_0 = \vec{k}_1 + \vec{k}_2, \quad (3)$$

and the temporal resonance one

$$\omega_0 = \omega_1 + \omega_2, \quad (4)$$

the nonlinear terms of Eq. (1) act as forcing terms transferring energy between the three waves. Since each wave must satisfy the dispersion relation (2), a finite amplitude, large length scale, high frequency wave (\vec{k}_0, ω_0) can transfer energy to produce two secondary waves of

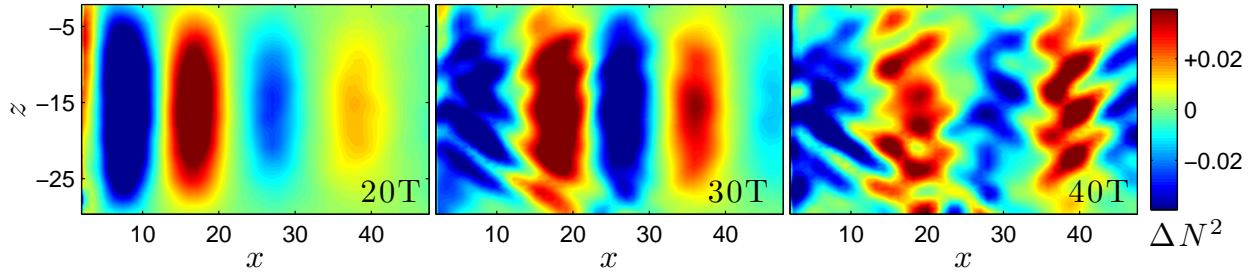


FIG. 1. (Color online) Snapshot of the horizontal density gradient (plotted as the square buoyancy frequency anomaly, in $\text{rad}^2 \cdot \text{s}^{-2}$) obtained at $t = 20T$, $t = 30T$ and $t = 40T$ with the parameters $a = 0.5$ cm, $\omega_0 = 0.95N$ and $N = 0.822$ $\text{rad} \cdot \text{s}^{-1}$.

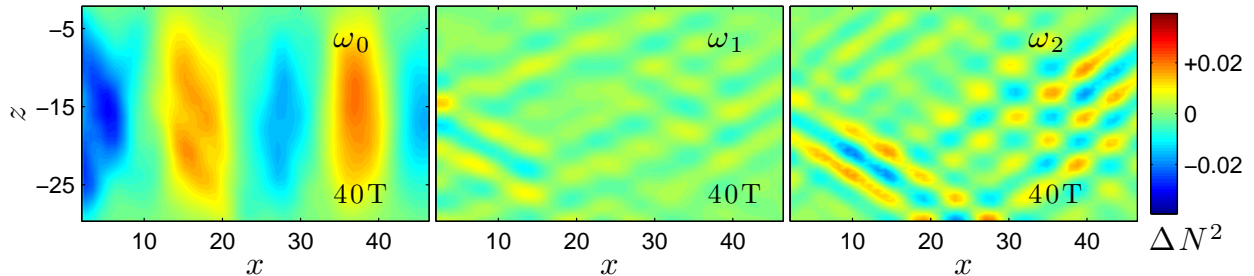


FIG. 2. (Color online) Real part of the Hilbert Transform of $\tilde{\rho}_x$ at $t = 40T$ (see Fig. 1(right)) presented after filtering at $\omega_0 = 0.95N$ (left), $\omega_1 = 0.38N$ (center) and $\omega_2 = 0.57N$ (right).

smaller length scales and lower frequencies, (\vec{k}_1, ω_1) and (\vec{k}_2, ω_2) .

The instability results from a competition between nonlinear effects and viscous dissipation. The growth is exponential if the amplitude of the secondary waves is initially small compared to the primary wave [12, 13]. The growth rate is then defined as

$$\lambda = -\frac{1}{2}(T_1 + T_2) + \left[\frac{1}{4}(T_1 - T_2)^2 + I_1 I_2 \psi_0^2 \right]^{1/2} \quad (5)$$

where ψ_0 is the amplitude of the stream function of the primary wave, I_1 and I_2 are the interaction coefficients

$$I_i = \frac{k_p m_q - k_q m_p}{2\omega_i \kappa_i^2} \left[\omega_i (\kappa_p^2 - \kappa_q^2) + k_i \left(\frac{k_p}{\omega_p} - \frac{k_q}{\omega_q} \right) \right] \quad (6)$$

where $i, p, q = 0, 1$ or 2 while $T_i = 1/2\nu\kappa_i^2$ is the viscous damping factor of the wave i and $\kappa^2 = k^2 + m^2$.

Experimental Configuration.—A tank, 160 cm long and 17 cm wide, is filled with linearly stratified salt water with constant Brünt-Väisälä frequency N using the double bucket system. The wave generator, similar to the one used in Ref. [14], is set to generate a monochromatic vertical mode-1, *i.e.* a horizontal velocity boundary forcing $u(x = 0, z, t) = -a\omega_0 \cos(\pi z/H) \cos(\omega t)$, H being the water depth, ω_0 the excitation frequency and a the amplitude of the oscillations of the plates of the wave-maker. The motion of the fluid is captured thanks to a Synthetic Schlieren technique using a dotted image behind the tank [15]. A camera is used to acquire images of this background at 1.875 frames per second. The CIV algorithm [16] computes the cross-correlation between

the real-time and the $t = 0$ background images, giving the variation of the horizontal, $\tilde{\rho}_x(x, z, t)$, and vertical, $\tilde{\rho}_z(x, z, t)$, density gradients.

Results.— Snapshots of an experimental horizontal density gradient field at different times for a particular experiment are presented in Fig. 1. At early times, a pure vertical mode-1 wave can be seen propagating to the right away from the wave generator located at $x = 0$: this is the *primary wave*. After several buoyancy periods (typically 30), this wave is destabilized and two *secondary waves* appear, of different frequencies and wave numbers from the primary wave. To see these waves more clearly, the horizontal density gradient at later times is filtered at the frequency of the primary wave, ω_0 and at the frequencies of the two secondary waves ω_1 and ω_2 . The result is shown in Fig. 2. It is clear that the mode-1 wave at $t = 40T$ is less intense than at $t = 20T$. Some of its energy has been transferred to both secondary waves. These two waves have smaller frequency and also smaller wavelength. In agreement with the dispersion relation, which links the frequency to the angle of propagation of the wave, the angle is different for the two wavelengths. Measuring the phase of the signal using a Hilbert transform [17], one can obtain the three different frequencies $(\omega_0, \omega_1, \omega_2) = (0.95, 0.38, 0.57)N$, attesting that the temporal resonance condition (4) is satisfied. Moreover, differentiating the phase, one measures the three wavevectors which are presented in Fig. 3. Within experimental errors, wave vectors satisfy the theoretical spatial resonance condition (3).

The measured density gradient fields are then analyzed using a time-frequency representation calculated at each

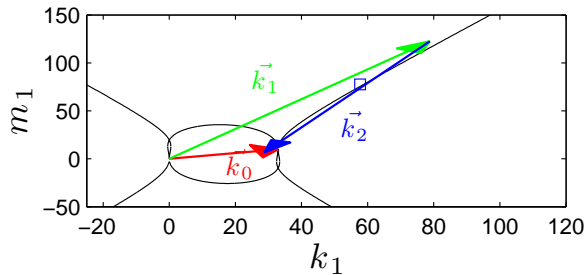


FIG. 3. (Color online) Spatial resonance conditions for the experiment presented in Fig. 1. The black line represents the location of the tip of the wave vector \vec{k}_1 for a given primary wave vector (\vec{k}_0) so that the resonance conditions (4) and (3) and dispersion relations (2) are satisfied. The three arrows are the experimental measurement of the three wave vectors: the red arrow is the primary wave vector \vec{k}_0 , the blue arrows the secondary wave vectors \vec{k}_1 and \vec{k}_2 . The box represents the most unstable theoretical mode.

spatial point [18]

$$S_x(t, \omega) = \left| \int_{-\infty}^{+\infty} du \tilde{\rho}_x(u) e^{i\omega u} h(t-u) \right|^2, \quad (7)$$

where h is a smoothing Hamming window of energy unity. A large (resp. small) window provides good frequency (resp. time) resolution. To increase the signal over noise ratio, data are averaged along a vertical line over the water depth. For large ω_0/N values, the dissipation length is small, so the analysis line is chosen to be close to the generator so that the amplitude is large.

Fig. 4(top) presents the spectra of the density field for four different amplitudes of the mode-1 wave with $\omega_0 = 0.94N$. The spectra is obtained using a large window to increase frequency resolution and by averaging $S_x(t, \omega)$ over the 10 last periods. Analyzing first the result for the amplitude 0.5 cm, the picture emphasizes a large peak close to 1 corresponding to the frequency of the mode-1 wave. A pair of twin peaks are observed, corresponding to secondary waves of frequencies, ω_1 and ω_2 , smaller than ω_0 .

The amplitude of each wave is then computed using a time-frequency analysis with a smaller window h . The amplitude of the secondary wave of frequency ω_1 is presented in Fig. 4(bottom). After a few buoyancy periods, a stationary state for the primary wave is reached. The secondary wave then starts to grow (except for the largest amplitude, where it starts very early) and a linear increase of the amplitude on a semilogarithmic plot is observed which confirms exponential growth. The value of the growth rate λ is measured using a linear fit, shown with the dashed lines in Fig. 4(bottom). The amplitude of the secondary waves finally saturates.

The influence of the amplitude of the wavemaker, and consequently of the primary wave, is presented for the same stratification and a forcing frequency of $0.94N$ in Fig. 4. The amplitude has an influence not only on the

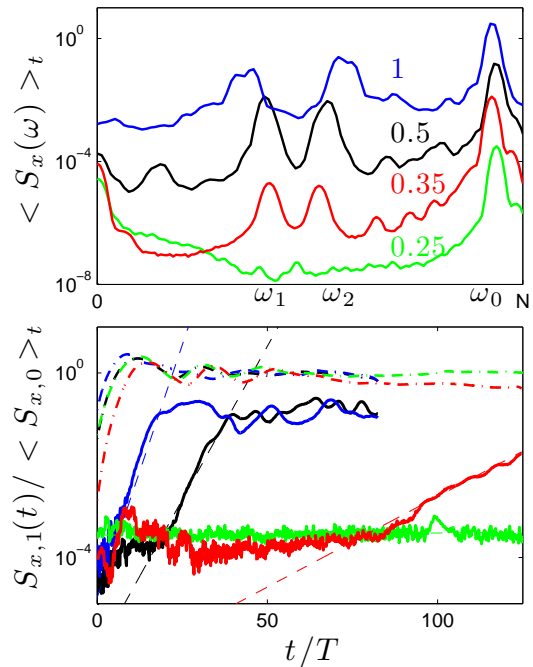


FIG. 4. (Color online) (Top) Spectra of the density gradient field, $\langle S_x(\omega) \rangle_t$, for four different amplitudes of the mode-1 for $\omega_0 = 0.94N$. The amplitudes are respectively 0.25 cm (green), 0.35 (red), 0.5 (black) and 1 (blue). The spectra 0.25, 0.35 and 1 are multiplied respectively by 0.01, 0.1 and 10 for illustration purposes. (Bottom) Amplitude of the secondary wave ω_1 , $S_{x,1}(t)$, normalized by the amplitude of the primary wave, $\langle S_{x,0} \rangle_t$, averaged over time when the steady-state of the mode-1 has been reached. Results are similar for the other secondary wave ω_2 . The dashed-dotted lines represent the amplitude of the primary wave, while the dashed lines shows the linear fit.

location but also on the height of the peaks of the secondary waves. If the amplitude of the primary wave is too small no peaks are visible and therefore no instability is observed attesting to the existence of an amplitude threshold. As the amplitude increases, the distance between the two peaks increases and the instability occurs earlier (after fewer buoyancy periods) and is stronger, *i.e.* with a larger growth rate. This result is in agreement with the theoretical growth rate (Eq. (5)).

Experiments were performed using the same stratification and an amplitude of 0.5 cm for frequencies in the range of $0.9 < \omega_0/N < 1$. For each experiment, the value of the frequencies of the two secondary waves, ω_1 and ω_2 , and the growth rate λ were measured. Experimental results are presented as a function of the frequency of the primary wave, ω_0/N , in Fig. 5. The sum of the frequencies of the two secondary waves, $\omega_1 + \omega_2$, is equal to the frequency of the primary wave, ω_0 , within experimental errors, in agreement with Eq. (4). As ω_0/N increases, the distance between the two secondary frequencies is larger. The measured value of the growth rate is presented in Fig. 5(right). The growth rate increases to reach a maximum around $\omega_0 = 0.95N$ and then decreases as ω_0 gets

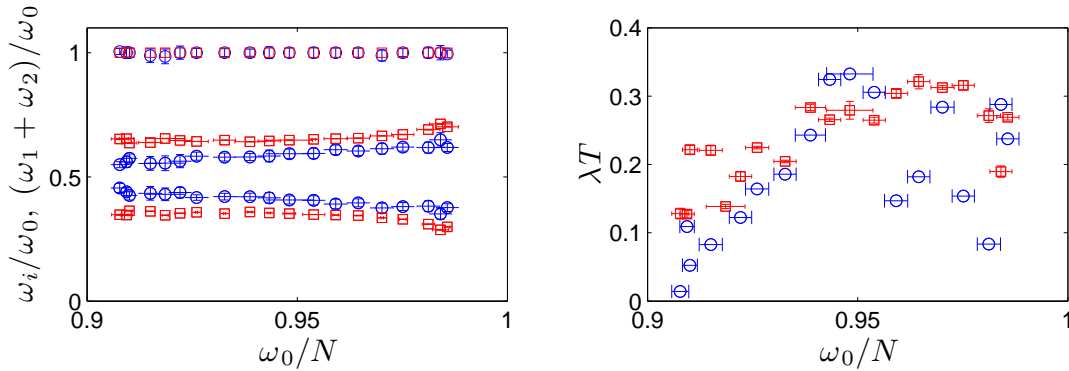


FIG. 5. (Color online) (Left) Values of the frequencies of the secondary waves for the experiments (blue \circ) and the theoretical calculation (red \square). The error bars are the width of the corresponding peak. The top line of point corresponds to the sum of the frequencies, with corresponding colors for theoretical and experimental data. (Right) Values of the growth rate of the secondary waves for the experiments (blue \circ) and the theoretical calculation (red \square). The theoretical values (\square) are computed using Eq. (5) and the measured amplitude of the primary wave.

closer to N .

To compare quantitatively the experimental results with the theoretical prediction of the growth rate, the value of the amplitude of the mode-1 wave has to be precisely known. The theoretical value of the amplitude of the streamfunction is equal to $a\omega_0/m_0$. However, as mentioned in [14], the conversion efficiency from the energy of the wavemaker to the energy of the mode-1 is less than unity and depends on experimental conditions. Moreover, as ω_0 gets closer to the cut-off frequency, N , the value of the viscous damping increases [19]. Consequently, the efficiency is not the same for all primary frequencies ω_0 , and the amplitude of the primary wave has to be measured experimentally to compute the theoretical value of the growth rate. It is important to check that the steady-state of the mode-1 wave has been reached. In contrast, the tank being finite in length, the measurement has to be performed before the mode-1 wave reflects back into the measurement area. Then, using a linear relation, the amplitude ψ_0 of the stream function at this particular frequency and wave number is $\psi_0 = g\omega_0\partial_x\tilde{\rho}_0/(k_0^2\bar{\rho}N^2)$. The theoretical frequencies of the instability is defined as the one that maximizes the growth rate. Without adjustable parameter, the comparison between experimental and theoretical results is presented in Fig. 5, emphasizing a good quantitative agreement.

Conclusions.— We have reported the first experimental measurement of resonant triad instability in stratified fluids and we have demonstrated this effect in a systematic set of laboratory experiments allowing careful comparisons with theoretical predictions. In practice, this heavily debated mechanism [11] has implications for many geophysical scenarios. Interestingly, although the generation mechanisms of oceanic IGW are quite well understood, their ultimate fate is currently poorly understood. Consequently determining the relative importance of parametric subharmonic instability, among the four recognized dissipation processes [1] is the next step

in furthering our understanding of how internal waves impact ocean mixing. Quantitative measurements of the subsequent mixing together with a fundamental study of wave turbulence would be of high interest.

Acknowledgements: The authors thank G. Bordes, P. Borgnat, B. Bourget, C. Staquet, for helpful discussions. This work has been partially supported by the PIWO grant (ANR-08-BLAN-0113-01).

-
- [1] E. Kunze, S.G. Llewellyn Smith, *Oceanography*, **17**, 55 (2004).
 - [2] B. Sutherland, *Internal Gravity Waves*, CUP (2011).
 - [3] P. Kumar *et al.*, *Astrophys. J.*, **520**, 859 (1999).
 - [4] G.N. Ivey, *et al.*, *Journal of Geophysical Research-Oceans*, **116** C01016 (2011).
 - [5] H. P. Zhang, B. King and H. L. Swinney, *Phys. Rev. Lett.*, **100**, 44504 (2008).
 - [6] M. Mathur and T. Peacock, *Phys. Rev. Lett.*, **104**, 118501 (2010).
 - [7] C. Staquet and J. Sommeria, *Ann. Rev. Fluid Mech.* **34**, 559 (2002).
 - [8] S. Thorpe, *J. Fluid Mech.* **32**, 489 (1969).
 - [9] A. McEwan, *J. Fluid Mech.* **50**, 431 (1971).
 - [10] D. Benielli, J. Sommeria, *J. Fluid Mech.* **374**, 117 (1998).
 - [11] D. Olbers, N. Pomphrey, *J. Phys. Ocean.*, **11**, 1423 (1981). J. MacKinnon, K. Winters, *Geophys. Res. Lett.*, **32**, L15605 (2005).
 - [12] C. Koudella, C. Staquet, *J. Fluid Mech.* **548**, 165 (2006).
 - [13] A.D. McEwan, R.A. Plumb, *J. Fluid Mech.* **55**, 589 (1977).
 - [14] L. Gostiaux *et al.*, *Exp. in Fluids* **42**, 123 (2007). M. Mercier *et al.*, *J. Fluid Mech.* **657**, 308 (2010).
 - [15] S. Dalziel, G.O. Hughes and B. Sutherland, *Exp. in Fluids* **28**, 322 (2000).
 - [16] A. Fincham, G. Delerce, *Exp. in Fluids* **29**:S1 (2000).
 - [17] M. Mercier *et al.*, *Phys. Fluids* **20**, 086601 (2008)
 - [18] P. Flandrin, *Time-Frequency/Time-Scale Analysis*, Academic Press, San Diego, 1999. Time-Frequency Toolbox for Matlab \circledR , <http://tftb.nongnu.org/>.
 - [19] P. Echeverri, M.R. Flynn, T. Peacock and K.B. Winters, *J. Fluid Mech.* **638** 91 (2009).